



Article

# Fabrication of Bimetallic High-Strength Low-Alloy Steel/Si-Bronze Functionally Graded Materials Using Wire Arc Additive Manufacturing

Marwan M. El-Husseiny <sup>1</sup>, Abdelrahman A. Baraka <sup>2</sup>, Omar Oraby <sup>2</sup>, Ehab A. El-Danaf <sup>1</sup>  
and Hanadi G. Salem <sup>2,\*</sup>

<sup>1</sup> Department of Mechanical Design and Production, Faculty of Engineering, Cairo University, Giza 12316, Egypt; marwan\_61@yahoo.com (M.M.E.-H.); edanaf@eng.cu.edu.eg (E.A.E.-D.)

<sup>2</sup> Additive Manufacturing Centennial Lab (AMCL), Mechanical Engineering Department, The American University in Cairo, Cairo 11835, Egypt; a.baraka@aucegypt.edu (A.A.B.); omaroraby@aucegypt.edu (O.O.)

\* Correspondence: hgsalem@aucegypt.edu

**Abstract:** In this paper, bimetallic functionally graded structures were fabricated using wire and arc additive manufacturing (WAAM). The bimetallic walls were built by depositing Si-Bronze and high-strength low-alloy (HSLA) steel, successively. The microstructural evolution of the built structures, especially within the fusion zone between the dissimilar alloys, was investigated in relation to their mechanical properties. The built bimetallic walls showed a high level of integrity. An overall interface length of 9 mm was investigated for microstructural evolution, elemental mapping and microhardness measurements along the building direction. Microhardness profiles showed a gradual transition in hardness passing through the diffusion zone with no evidence for intermetallic compounds. Failure of the tensile specimens occurred at the Si-Bronze region, as expected. Bending tests confirmed good ductility of the joint between the dissimilar alloys. Direct shear test results proved a shear strength comparable to that of HSLA steel. The obtained results confirm that it is appropriate to fabricate HSLA steel/Si-Bronze FGMs using WAAM technology.

**Keywords:** wire arc additive manufacturing; functionally graded materials; copper–steel bimetallic components; pulsed gas metal arc welding



**Citation:** El-Husseiny, M.M.; Baraka, A.A.; Oraby, O.; El-Danaf, E.A.; Salem, H.G. Fabrication of Bimetallic High-Strength Low-Alloy Steel/Si-Bronze Functionally Graded Materials Using Wire Arc Additive Manufacturing. *J. Manuf. Mater. Process.* **2023**, *7*, 138. <https://doi.org/10.3390/jmmp7040138>

Academic Editors: Mohsen K. Keshavarz and Esmail Sadeghi

Received: 1 July 2023  
Revised: 23 July 2023  
Accepted: 25 July 2023  
Published: 31 July 2023



**Copyright:** © 2023 by the authors. Licensee MDPI, Basel, Switzerland. This article is an open access article distributed under the terms and conditions of the Creative Commons Attribution (CC BY) license (<https://creativecommons.org/licenses/by/4.0/>).

## 1. Introduction

Intelligent, connected, and decentralized manufacturing plants are being developed depending on the advances in computational intelligence together with recent developments in manufacturing technologies so that optimized production flows and higher efficiencies can be achieved under the umbrella of the fourth industrial revolution (Industry 4.0). As a non-traditional manufacturing approach, additive manufacturing (AM) has a vital role in Industry 4.0. Among many advantages, the environmental impact of AM is very impressive as it offers improved sustainability in production systems compared to traditional manufacturing methods. One of the main purposes of using AM is to accelerate prototyping and reduce the production time for spare and replacement parts [1–3].

Wire and arc additive manufacturing (WAAM) is a promising technology that uses wire feedstock and an arc welding power source integrated with a robotic manipulator to fabricate complex near-net-shape integral metal parts. Compared to alternative AM technologies, WAAM has the merits of its high deposition rate, lower feedstock material cost, capability to manufacture medium- to large-scale components, and flexibility to integrate with subtractive manufacturing technologies, creating a hybrid manufacturing facility [4,5]. Unmanned WAAM workshops can be realized efficiently with the development in the concepts of Industry 4.0 and Internet of Things [6]. Several studies have been published regarding online process monitoring and post-processing methods in order to achieve

the desired dimensions of WAAM-fabricated components [7–9]. WAAM is a versatile process that can be implemented in manufacturing functionally graded material (FGM) parts with innovative designs in a cost-effective fashion [10]. FGMs have the ability to resolve material selection challenges in current industrial applications via customizing material properties based on application performance demands [11]. FGM parts can be additively manufactured using a single material with different microstructures between layers with the process parameters changed during fabrication [12]. Such parts can be built from a large variety of materials by combining different wires, or even wires with metallic powders from a separate feeder during a single build [13]. They may be entirely produced additively by depositing multiple layers of dissimilar metallic materials, or a pre-fabricated metallic part may act as the substrate for subsequent additive fabrication with a different metal [14].

Among FGM combinations that can be fabricated using WAAM, copper–steel functionally graded bimetallic parts are of major interest in rocket nozzle engines, heat transfer components, the cryogenic sector, electric conductors, power generation, and die-casting [11]. When used in die-casting, the high thermal conductivity of copper allows an intense heat extraction from the castings, which reduces the production times and manufacturing costs and refines the microstructure by promoting faster cooling rates. Copper and its alloys offer good wear and corrosion resistance, while steel provides excellent toughness and fatigue properties [15]. Technologies that connect copper and steel not only aim to take full advantage of the two materials, but also to improve the comprehensive economic benefits of the bimetallic parts. Therefore, copper–steel FGM has broad application prospects in industrial engineering [15–18].

Despite the mentioned advantages and application fields for copper–steel FGM, several challenges may hinder a successful joint between the two dissimilar metals. The mismatch in their thermal expansion coefficients results in large misfit strains and, consequently, high residual stresses [15]. Copper conducts heat energy up to 10 times faster than steel, tending to dissipate heat rapidly away from the weld pool, leading to difficulties in reaching the melting temperature of copper [17]. Moreover, the Fe-Cu phase diagram exhibits a large miscibility gap, preventing the favorable formation of solid solutions between both metals upon cooling [15]. Another major problem in joining the two dissimilar alloys is hot cracking in the heat-affected zone (HAZ) of steel due to copper penetration into the grain boundaries of steel [17].

Copper–steel FGM has already been fabricated using different additive manufacturing technologies; however, only a few researchers have studied its fabrication using WAAM process. Rodrigues et al. [15] used twin WAAM (T-WAAM) based on gas tungsten arc welding (GTAW) to deposit a copper–aluminum alloy (ERCuAl-2-A2) and high-strength low-alloy steel (ER120S-G) FGM walls along with control specimens of the unmixed metals. Microstructural investigation revealed  $\delta$ -ferrite and  $\epsilon$ -copper as the primary phases in the relatively large interfacial region (12 mm) with an absence of intermetallic species. Tensile tests produced a combination of 690 MPa of strength with 16.6% fracture elongation. Fracture occurred in the copper region away from the interface, indicative of the mechanical integrity of the interfacial zone. Tomar and Shiva [19] employed cold metal transfer (CMT) based WAAM to fabricate stainless steel (AISI 316L) and copper bimetal. The diffusion of iron species into the copper region was observed up until the third deposited copper layer (with a reported interface length of 5 mm), where the uniformity of iron distribution was higher compared to that in the first layer. The primary morphologies that were assumed by the diffusing species were that of globular and dendritic iron, being dominantly present in the first and subsequent layers, respectively. Moreover, the segregation of copper atoms into globular iron morphology but not in the dendritic was noted. Liu et al. [16] utilized gas metal arc welding (GMAW)-based WAAM to prepare mild steel Si-Bronze bimetal. Tensile testing revealed an intact interface between both material regions, with fracture occurring near the interface on the copper side after reaching a maximum strength of 305 MPa. The interface was shown to be primarily dominated by ferrite and  $\epsilon$ -copper phases. Zhang

et al. [18] investigated the effect of adding a Cu-Ni interlayer between the depositions of steel and Si-Bronze on the mechanical properties of the bimetallic material. ER50-6 low-alloy steel was used along with HS211 Si-Bronze and prepared using GMAW-based wire arc additive manufacturing. The insertion of an interlayer was noticed to increase the tensile strength by 66.36%, reaching 345.2 MPa. This enhancement was attributed to the facilitated diffusion of elements in the interfacial region upon adding the Cu-Ni layer, thereby suppressing the onset of micro-cracking in this region. Tensile testing of the sample without the interlayer showed fracture at the interface.

In this study, bimetallic HSLA steel/Si-Bronze structures were fabricated using pulsed-GMAW-based WAAM. The challenges in joining the two dissimilar alloys are addressed. The microstructural evolution of the built structures, especially within the fusion zone, was investigated in relation to their mechanical properties. Several mechanical tests were performed to confirm the integrity of the interface.

## 2. Materials and Methods

### *Material Used and Building Strategy*

WAAM was carried out using a GMAW power source of the type Fronius TransPuls Synergic 4000 (TPS 4000). The reproducible guidance of the welding torch was realized using a 6-axis industrial robot ABB IRB 1600 (1.2 m reachability) and a 2-axis positioner ABB IRBP A-type where the substrate is fixed. Figure 1 shows the additive/subtractive manufacturing integrated robotic system at the Additive Manufacturing Centennial Lab (AMCL) located in The American University in Cairo.



**Figure 1.** The additive/subtractive robotic-controlled manufacturing system, AMCL [20].

Two 1.2-mm-diameter filler wires were used successively for the deposition of the bimetallic structures, namely ER110S-G and ERCuSi-A. The chemical compositions of the filler wires are listed in Table 1, according to the manufacturers' datasheets. A mild steel substrate was used with the dimensions  $250 \times 250 \times 15$  mm. Three different types of walls were fabricated: (i) unmixed HSLA steel walls, (ii) unmixed Si-Bronze walls, and (iii) bimetallic HSLA steel/Si-Bronze walls. Three walls were built for each condition to ensure repeatability of the process. All deposited structures were thin walls with average dimensions of 160 mm length, 120 mm height, and 8.5 mm width.

**Table 1.** Filler wires’ chemical compositions (wt.%) (all single values are maximums).

ER110S-G, Diameter: 1.2 mm	Fe Bal.	C 0.068	Cr 0.3	Si 0.54	Cu 0.21	V 0.086	Mo 0.2	Mn 1.55	P 0.009	S 0.014	Ni 1.48
ERCuSi-A Diameter: 1.2 mm	Cu Bal.	Zn 1	Sn 1	Si 2.8–4.0	Fe 0.5	Al 0.01	Mo -	Mn 1.5	Pb 0.02	S -	Other 0.5

The build strategy of the bimetallic walls is illustrated in Figure 2, where HSLA steel was initially deposited on the mild steel substrate then Si-Bronze was deposited on the previously deposited HSLA steel layers. Two beads per layer were deposited for the HSLA steel with an overlap percentage (OP) of 40% (Figure 2b), while one bead per layer was used while depositing the Si-Bronze (Figure 2c) so that the difference in bead width (BW) between the two deposited materials is compensated for. Two beads per layer with 40% OP would result in a calculated bead width of 8 mm, given that the single bead width is 5 mm, according to the processing parameters shown in Table 2. However, after depositing 38 layers of HSLA steel, an average bead width of 8.5 mm was realized. The authors relate the increase in the average bead width to the increase in the number of layers as a result of heat accumulation after successive depositions. For Si-Bronze, a higher heat input is used to compensate for its fast heat dissipation, such that one bead of Si-Bronze would cover two beads of HSLA steel, as shown in Figure 2c.

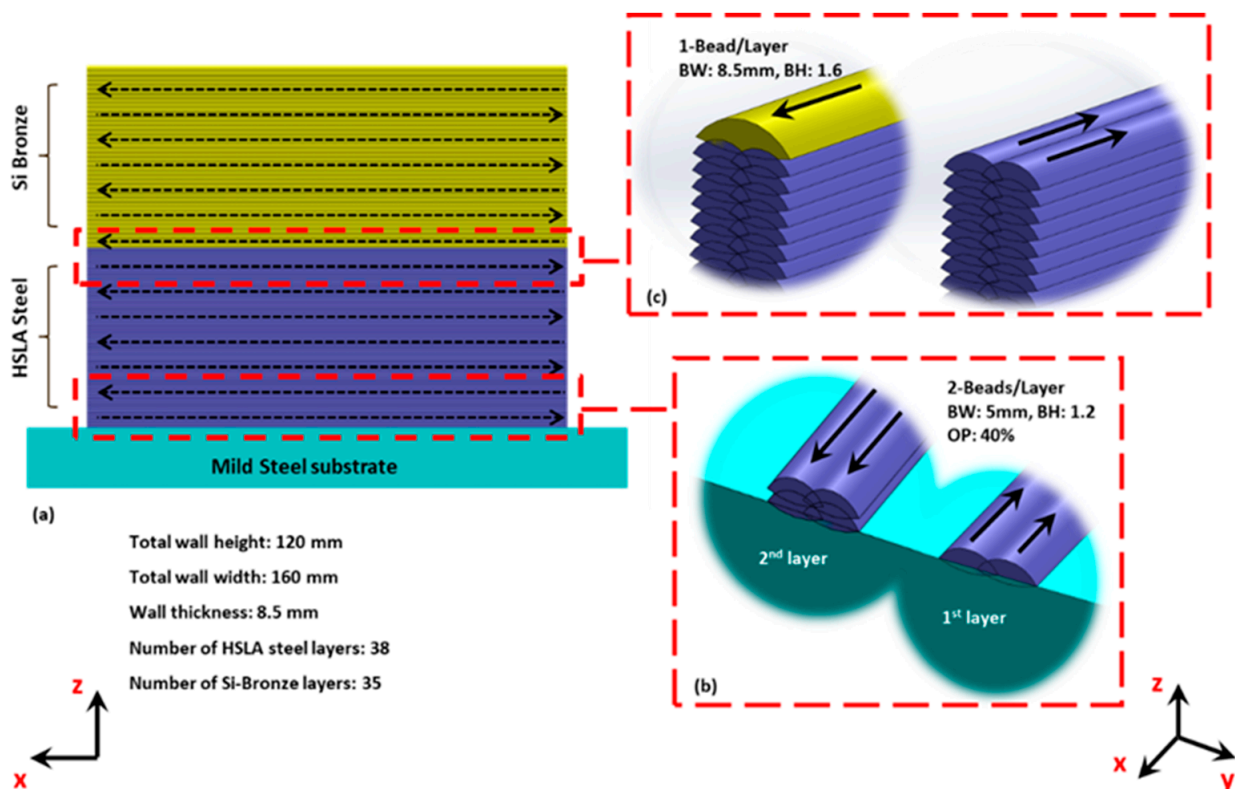


**Figure 2.** (a) Schematic for the deposited FGM walls and their deposition strategy, (b) schematic showing the first deposited HSLA steel overlapping double beads on the mild steel substrate, and (c) schematic for the first deposited Si-Bronze single bead on the HSLA steel wall.

A single-path alternating strategy was used for all depositions, such that each layer is deposited in an opposite direction to the previous one, as shown in Figure 2. The alternating strategy results in more even thermal distribution across the deposited walls, aiming at enhancing wall geometrical uniformity, especially at the wall ends.

Table 2 summarizes the WAAM processing parameters for the HSLA steel and Si-Bronze materials. The current used to deposit Si-Bronze was set to a higher value than that used to deposit HSLA steel owing to the higher thermal conductivity of the copper-based alloy, which tends to dissipate heat rapidly [21]. The bead temperature was measured after the deposition of each layer using a handheld AMPROBE IR-750-EUR thermal gun to ensure that the maximum temperature was lower than the specified interpass temperature. The interpass temperature for HSLA steel deposition was 120 °C, while that of the Si-Bronze was 100 °C. The temperature of the last deposited bead was considered upon measuring the interpass temperature. The first HSLA steel layer was deposited on a cold mild steel substrate and, similarly, the first Si-Bronze layer was deposited while the HSLA steel top layer was kept at room temperature. Neither pre-heating nor forced cooling were applied.

The heat input corresponding to the deposition parameters of each material is presented in Table 2, and it was calculated according to the following formula [22]:

$$H_{in} = (V \times I/TS) \times \eta \tag{1}$$

where  $H_{in}$  is the heat input per unit length,  $V$  is the welding voltage,  $I$  is the welding current,  $TS$  is the travel speed, and  $\eta$  is the process efficiency, which is considered 0.8 according to Elsokaty et al. [20]. The layer geometry, microstructure, and hardness of WAAM parts strongly depend on the heat input. Therefore, heat input is a major parameter in the WAAM process and should be selected carefully to achieve a sound deposition. Less heat input results in a faster cooling rate and therefore finer microstructure, leading to higher hardness values. The deposited material volume per unit length (DMV) is listed in Table 2, corresponding to the processing parameters for each material, and it was calculated according to the following formula [22]:

$$DMV = WFS \times A_w/TS \tag{2}$$

where  $WFS$  is the wire feed speed and  $A_w$  is the wire cross-sectional area. The welding current is directly proportional to  $WFS$  and the wire cross-sectional area. Therefore, DMV is directly proportional to the heat input. DMV represents the volume of molten metal that is deposited over a unit length of the previously deposited layer or the substrate. The material deposition rate (DR) is presented in Table 2, corresponding to the processing parameters for each material, and it was calculated according to the following formula [23]:

$$DR = WFS \times A_w \times \rho \tag{3}$$

where  $\rho$  is the mass density of the filler wire material (7800 kg/m<sup>3</sup> and 8750 kg/m<sup>3</sup> for HSLA steel and Si-Bronze, respectively). The deposition rate denotes the quantity of material deposited per unit time, which is a measure of the process productivity.

**Table 2.** WAAM processing parameters.

	HSLA Steel	Si-Bronze
Wire feed rate (m/min)	2.5	6.7
Current (A)	80	193
Voltage (V)	18.9	23.1
Welding mode	Pulsed—GMAW	
Travel speed (mm/s)	6	12
Shielding gas	82%Ar + 18%CO <sub>2</sub> @15 L/min	99.9% Ar @15 L/min
Interpass temperature (°C)	120	100
Heat input (J/mm)	200	300
DMV (mm <sup>3</sup> /mm)	7.85	10.52
DR (kg/h)	1.32	3.98

### 3. Characterization and Testing Techniques

#### 3.1. Microstructural Evolution

Cross sections were cut from three different walls using wire EDM technology for the purposes of micrographic examination and mechanical testing, as shown in Figure 3, which depicts the locations of the samples cut. Table 3 describes the tags and dimensions of the characterization samples.

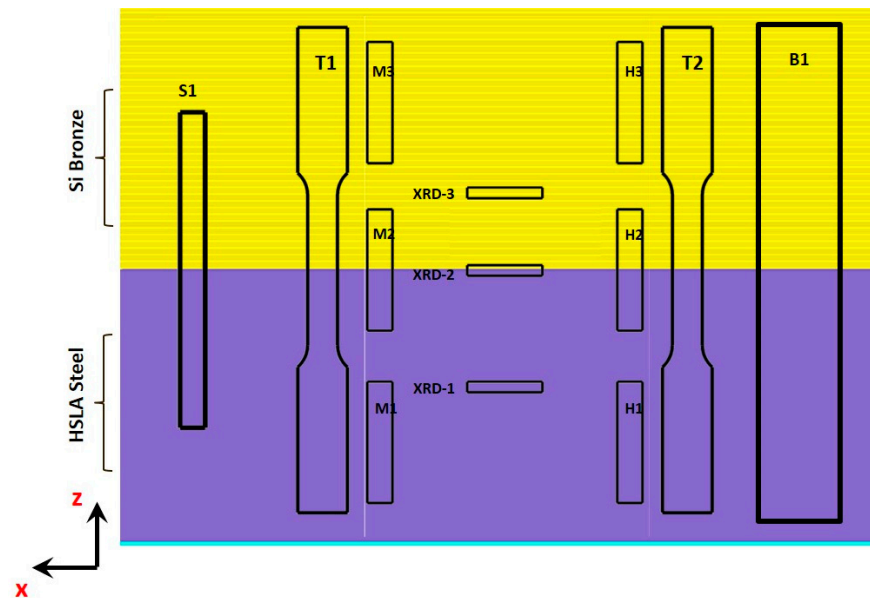


**Figure 3.** Schematic representation of the characterization samples cut from the deposited functionally graded material of HSLA steel/Si-Bronze walls.

**Table 3.** Description of the test samples tags.

Tag	Description
T1, T2	Tensile samples (ASTM E8/E8M, gauge length: 25 mm, thickness 5 mm)
S1	Shear sample (diameter: 5 mm, height: 60 mm)
B1	3-point bending sample (length: 110 mm, width: 40 mm, thickness: 5 mm)
H1–H3	Micro-hardness samples (length: 25 mm, width: 5 mm, depth: 10 mm)
M1–M3	Microstructure, SEM/EDS samples (length: 25 mm, width: 5 mm, depth: 10 mm)
XRD-1 to XRD-3	X-ray diffraction samples (length: 10 mm, width: 5 mm, thickness: 2 mm)

Microstructure analysis was carried out on samples to include the plain HSLA steel and Si-Bronze going through the diffusion zone along the building direction. The samples were ground using a series of grinding SiC paper up to 4000#. Polishing was carried out using diamond suspension 1 μm at a speed of 200 rpm. Si-Bronze specimens were etched using an iron (III) chloride (5 g) with ethanol and HCl. Etching of HSLA steel specimens was carried out using 4% Nital mixture. Specimens taken from the interface zone containing both metals were meticulously screened during the application of either etchant to avoid over-etching. Optical micrographs were acquired using bright-field illumination using a Zeiss AxioImager2 upright microscope. A JEOL JSM-6010 scanning electron microscope (SEM) equipped with an integrated energy dispersive X-ray spectroscope (EDS) was also used for microstructural characterization and elemental analysis. X-ray diffraction (XRD) patterns were determined for the HSLA steel, interface, and copper regions using a BRUKER D8 Discover (Billerica, MA, USA). Multiple scans were carried out for different locations along the build direction for both HSLA steel and Si-Bronze passing through the diffusion zone (interface) to investigate the evolution of different phases in each metal.

### 3.2. Mechanical Properties Characterization

The mechanical integrity of the walls was confirmed using micro-hardness, uniaxial tensile, three-point bending, and direct single shear tests. Samples were cut using wire EDM, as illustrated in Figure 3.

Microhardness testing was carried out on samples cut from the walls in varying locations along the HSLA steel and Si-Bronze regions passing through the fusion zone using a DuraScan 20 G5 hardness testing machine (Zwick/Roell, Kuchl, Austria), with a force of 10 N and a dwell time of 10 s.

Tensile tests were performed on (i) unmixed HSLA steel samples, (ii) unmixed Si-Bronze samples, and (iii) HSLA steel/Si-Bronze bimetallic samples. The bimetallic tensile samples were cut such that the interface between the HSLA steel and Si-Bronze samples was at the middle of the gauge length. Tensile tests were carried out at room temperature according to the ASTM E8/E8M standard with a gauge length of 25 mm and a thickness of 5 mm, using an INSTRON 3382 universal testing machine at a crosshead speed of 2 mm/min. The same machine was used for the three-point bending test to assess the integrity of the joint between the two dissimilar alloys. The tested bimetallic specimens were simply supported at the ends and the load was gradually applied normal to the interface until fracture or reaching a maximum specified displacement of 30 mm, as illustrated in Figure 4. The span length was fixed at 63 mm and the specimens' dimensions were 40 mm width, 5 mm thickness, and 110 mm length. Flexural strength is calculated according to the following formula [17]:

$$\sigma_f = 3 P_u L / 2 b d^2 \tag{4}$$

where  $\sigma_f$  is the flexural strength,  $P_u$  is the applied load,  $L$  is the span length ( $L = 63$  mm),  $b$  is the specimen width ( $b = 40$  mm), and  $d$  is the specimen thickness ( $d = 5$  mm). Dye penetrant testing was performed before and after bending to examine the effect of bending stresses on the tensioned side of the interface.

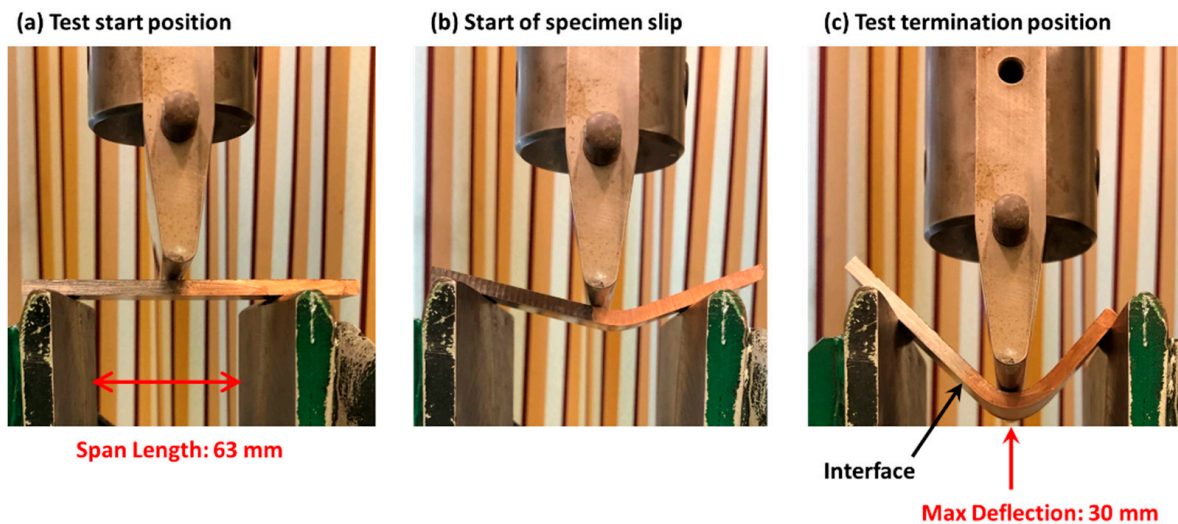


Figure 4. Three-point bending test setup.

Direct single shear testing was performed on the interface between the two dissimilar metals. Samples were cut from as-deposited bimetallic walls and they were turned to a 5 mm diameter. The shear test setup and specimen are shown in Figure 5. The shear strength of the interface is calculated according to the following formula [17]:

$$\tau = P_{max} / A_{sp} \tag{5}$$

where  $P_{max}$  is the maximum shear load and  $A_{sp}$  is the cross-sectional area of the tested specimen.

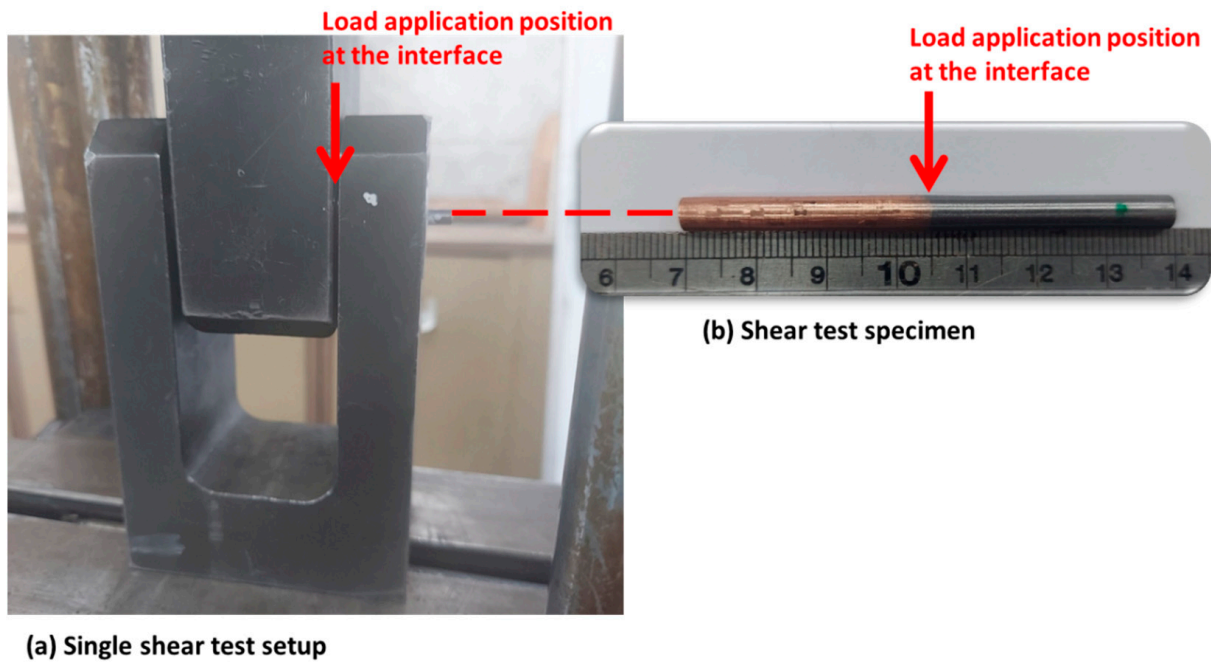


Figure 5. (a) Direct single shear test setup and (b) shear test specimen.

#### 4. Results and Discussion

##### 4.1. Macroscopic Characterization

A sample of the deposited bimetallic walls before and after machining is shown in Figure 6. The macroscopic inspection showed a smooth transition between successive layers with no evidence of irregularity or collapse. Additionally, there was no evidence for macro-porosities or interlayer cracking, which is indicative of the walls' integrity, associated with the suitable deposition parameters.

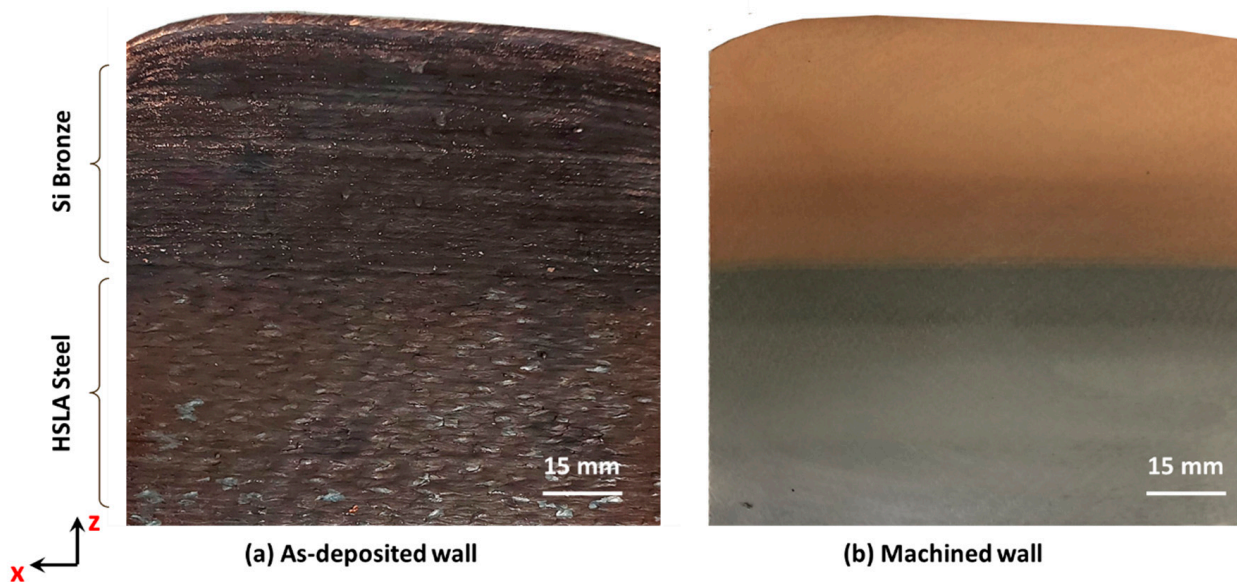
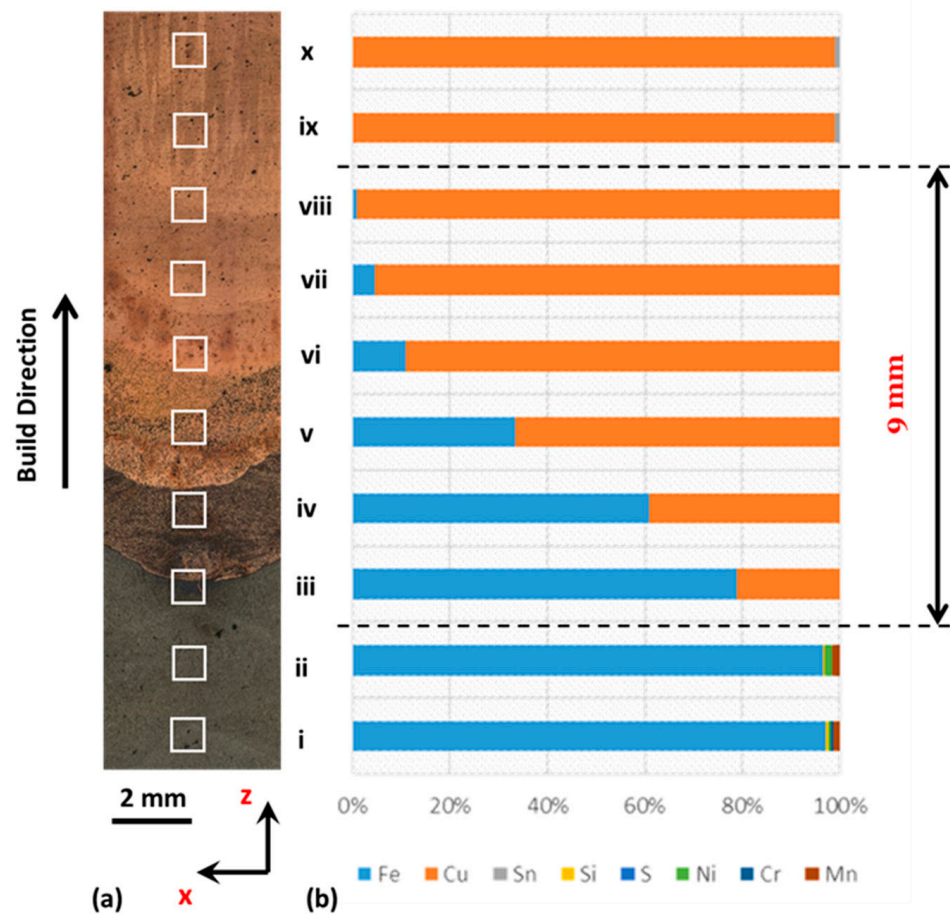


Figure 6. A sample of the deposited walls (a) as-WAAM-ed and (b) after machining.

##### 4.2. Microstructure Evolution

A panoramic image of the interface region (sample "M2" in Figure 2) is presented in Figure 7a, where the microstructures developed within the HSLA steel, fusion zone, and the Si-Bronze deposited layers are depicted. Elemental distribution along the height of the

interface was determined using EDS spectrum analysis at ten locations with an increment of 1.5 mm, as presented in Figure 7b.



**Figure 7.** (a) Panoramic image of the interface cross section and (b) a bar chart showing the corresponding elemental distribution for each of the ten shown locations (i–x) along the build direction.

It can be seen that the first two locations (i, ii) are free from copper element, indicating the dominance of HSLA steel. A high-magnification scanning electron micrograph together with EDS elemental mapping of the HSLA steel region is presented in Figure 8. A martensite–austenite (MA) phase is observed in a matrix of  $\alpha$ -ferrite, in accordance with [15]. The presence of MA constituents in low-alloyed steel is attributed to incomplete transformation of austenite into martensite during multiple reheating cycles to critical temperatures. The interfacial boundary between HSLA steel and Si-Bronze is illustrated in Figure 9 together with elemental distribution of the iron and copper. Insufficient mixing between iron and copper is realized at the interface boundary, which can be attributed to the miscibility gap between both metals, as presented in the phase diagram in Figure 10 [24]. Figure 11 presents SEM micrographs coupled with the corresponding EDS elemental area mapping of the interface (Figure 7, location [iii] to location [x]). A micro-crack originating in the diffusion zone of the first deposited Si-Bronze layer is evident in location (iii). The micro-crack is manifested in Figure 11p–r, where the elemental mapping depicts the Cu element diffusion within the crack while in the liquid state prior to solidification, indicative of the formation of a hot crack within the HSLA steel layer. It is suggested that depositing the first Si-Bronze bead on the cold HSLA steel one resulted in a thermal shock associated with hot cracking [14]. The penetration of the Si-Bronze within the crack during the bead deposition acted as a self-healing process to the expected stress concentration that could have initiated failure under loading. This will be evident in the following section, which reports on the mechanical behavior of the built FGM. The first interface layer of Si-Bronze is

depicted in Figure 11 (iv, v), where iron predominantly solidified in globular and dendritic morphologies [15,16,18,19,24]. EDS scans of further locations in the copper region along the deposition direction indicate that the diffusion of iron element was extended up to the fifth deposited Si-Bronze layer, with progressive reduction in content after the second layer.

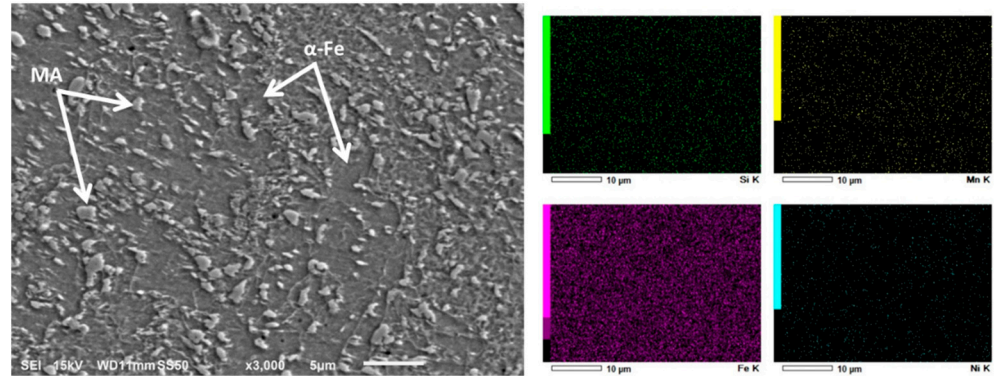


Figure 8. SEM micrograph (left) together with EDS mapping (right) for HSLA steel locations (i, ii).

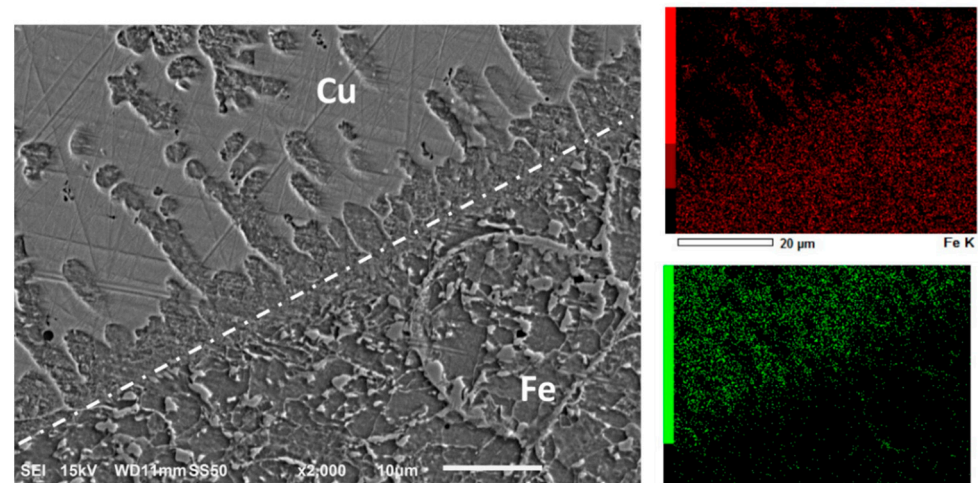


Figure 9. SEM micrograph together with EDS elemental area mapping of the intermixing zone along the interface boundary.

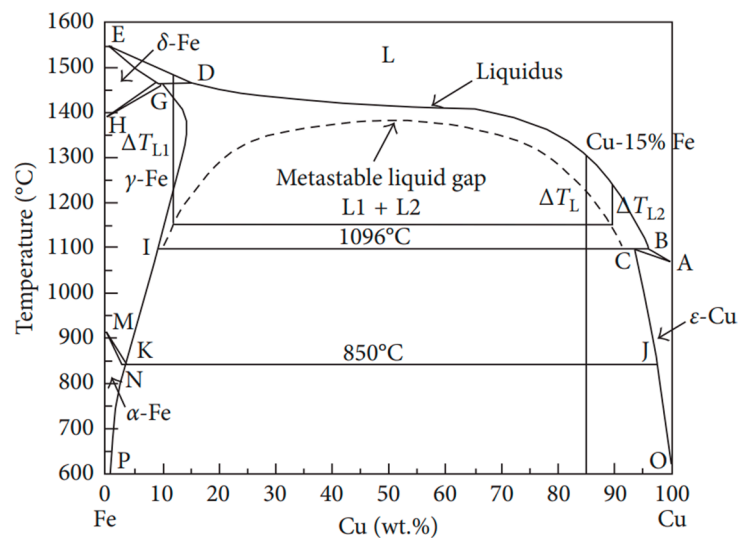
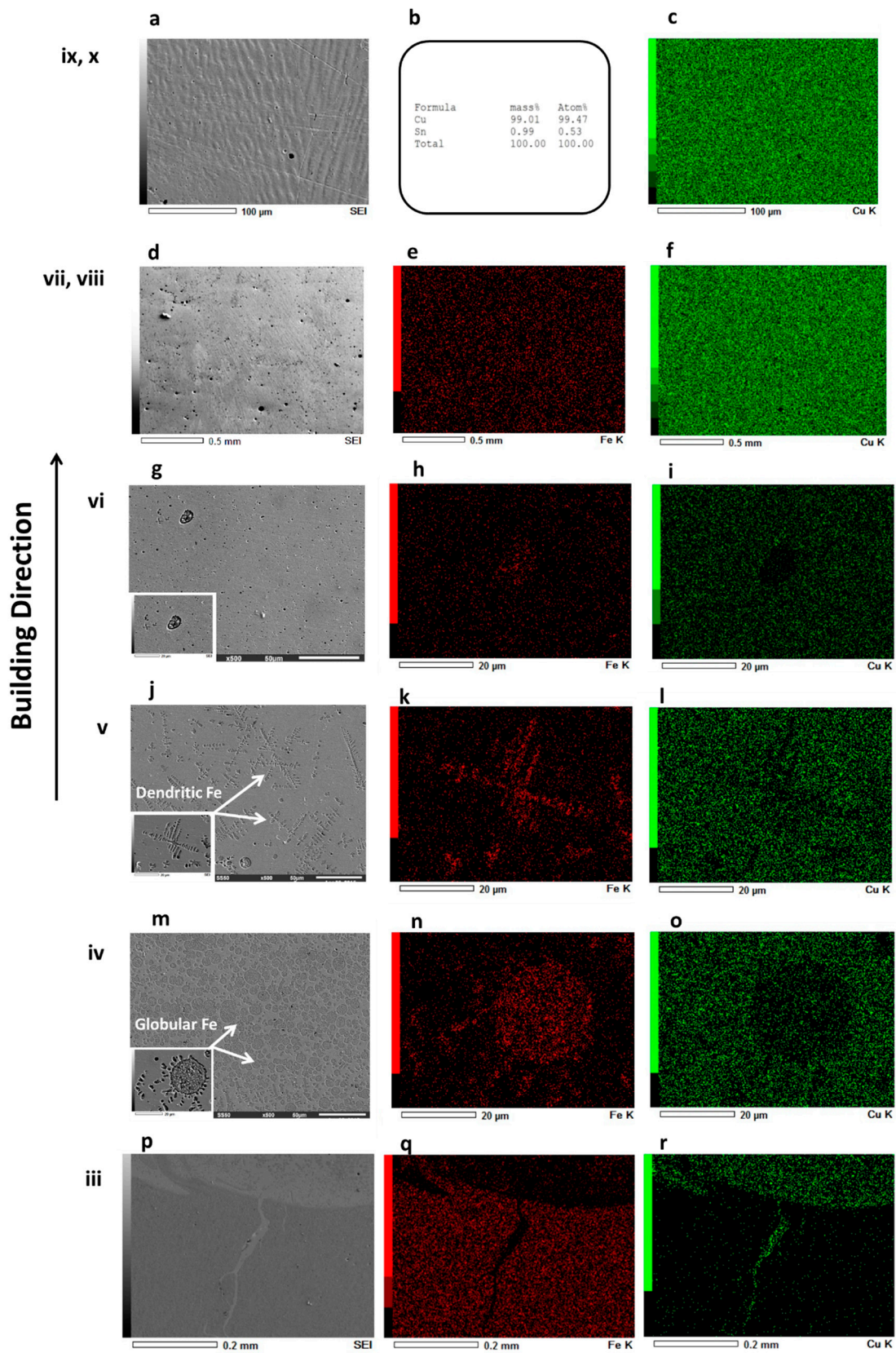


Figure 10. Iron-copper phase diagram showing the wide miscibility gap between both metals [24].



**Figure 11.** SEM images together with elemental mapping of formed structures between HSLA steel and Si-Bronze along the building direction pointed out by the arrow on the left-hand side of the figure; (a–c) locations x and ix; (d–f) locations viii and vii; (g–i) location vi; (j–l) location v; (m–o) location iv; (p–r) location iii.

In terms of the morphological distribution of iron within the copper region, the interface can be roughly divided into three portions: the first one is the layer directly above the latest HSLA steel deposited layer, where there is a tendency of iron to consolidate in the form of both dendritic and globular formations, which can be explained on the basis of the complex thermal gradients and histories arising at the deposition of the first copper layer on the cold steel surface [19]. The second portion above it (top of first Si-Bronze layer) mainly contains iron globules with no apparent dendritic formation. The third region (second Si-Bronze layer) shows decreased iron diffusion density and the inclination to form dendritic arrangements. Starting from the sixth deposited layer, no iron diffusion can be considered, and the morphology of copper is changed to columnar owing to the effect of directional thermal gradient. The interface region is defined as the region of intermixing species of iron and copper and consists of approximately five layers of subsequent copper depositions onto the steel wall. This results in an overall interface length of 9 mm. This value lies between the ones obtained in [15,19], which correspond to 5 and 12 mm, respectively.

#### 4.3. XRD

XRD analysis confirmed the diffusion of iron globules into the copper side, as shown in Figure 12b. The interface region is observed to contain both metals of the bimetallic component, with iron occurring predominantly in its ferritic phase, while copper is in its FCC  $\epsilon$ -phase. This observation is consistent with the works of [16,18]. Furthermore, the deposition of the first copper layers on the cold steel wall favored copper grain nucleation compared to grain growth and led to the subsequent solidification of finer copper grains. This can be ascribed to the high undercooling that resulted from the large temperature gradient between liquid copper and steel. Subsequent deposition exhibited columnar grain growth due to the reduction in undercooling and the formation of a directional temperature gradient along the build direction, as can be observed in Figure 12c. The XRD peak intensity is consistent with this suggestion, where the intensity of the peaks in the unmixed copper region are lower compared to their finer counterparts in the interfacial region [19]. No intermetallic phases were formed in the interfacial region. The absence of intermetallic compounds was also observed in [15,16,18]. Moreover, the analysis is in good agreement with the OM, SEM, and EDS results and highlights the feasibility of fusing both candidate materials together with no adverse generation of metastable species. No phase variation with height was observed.

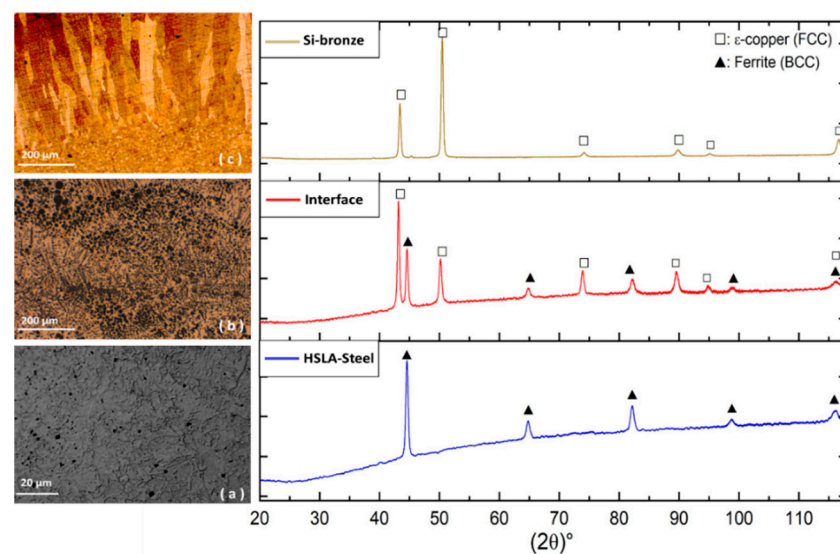


**Figure 12.** XRD analysis in different regions along the build direction together with the corresponding microstructures: (a) HSLA steel region, (b) fusion zone, (c) Si-Bronze region.

#### 4.4. Hardness Measurements

Figure 13 represents the micro-hardness values of the interface (specimen H2 in Figure 2) in the form of a color map together with a panoramic image showing the corresponding microstructures. The samples showed a smooth hardness profile with strong agreement with the previously presented XRD and microscopy results. The hardness values for HSLA steel were found in the range of 220–260 HV with a bottom-up descending trend. The highest hardness value was determined in the lower plain HSLA steel region, while the lowest was close to the interface boundary. The decrease in the HSLA steel hardness near the interface is attributed to the increase in Cu content together with the coarsening of the Fe (BCC) grains near the interface as a result of the higher heat input of the deposited Si-Bronze layers and, consequently, lower cooling rates in this region. Similar hardness values were reported by Rodriguez et al. [15]. The hardness values at the top of the first diffusion layer (130–180 Hv) are higher than those of the plain Si-Bronze due to the iron diffusion and formation of ferritic phases (Figure 11 (iv, v) and Figure 12). Crossing the interface boundary towards the Si-Bronze copper-rich region (location iv), the average hardness value decreased to 155 HV. At location v, an average hardness of 120 HV was recorded. A continuous descending trend of the hardness values was evident owing to the decrease in Fe-BCC constituents in the microstructure, coupled with the dominance of the Si-Bronze, until reaching a minimal average value of 65 HV in the coarse columnar grains of the plain Si-Bronze upper layers. The micro-hardness measurements did also attest to the previously claimed interface height of 9 mm based on the gradual transition between the HSLA steel hardness values and those of Si-Bronze. The micro-hardness profile did also prove the absence of intermetallic compounds within the interface boundary between the two dissimilar alloys.

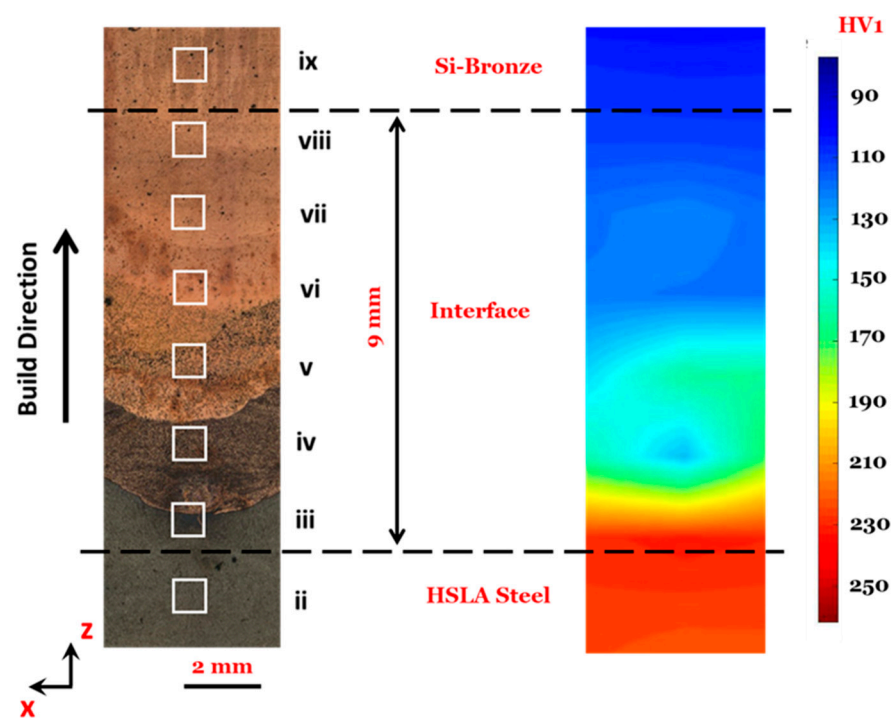
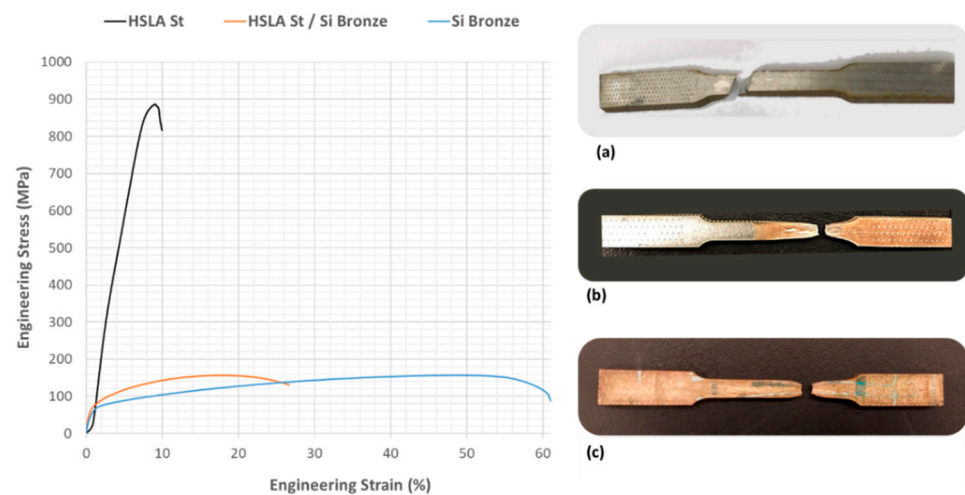


Figure 13. Micro-hardness color contour shown on the right of the interface microstructure.

#### 4.5. Uniaxial Tensile Test

The tensile tests were performed on three WAAM-ed samples: (a) unmixed HSLA steel, (b) HSLA steel/Si-Bronze FGM, and (c) unmixed Si-Bronze. Figure 14 depicts the engineering stress–strain curves confirming that the tensile properties of the FGM are indeed a combination of the properties of both parent materials. Unmixed HSLA steel

exhibits a tensile strength of 950 MPa with a ductility of less than 10%, whereas Si-Bronze demonstrates 150 MPa strength with more than 60% fracture elongation. For the functionally graded material of HSLA steel and Si-Bronze, the tensile strength attained was around 160 MPa, with an elongation at fracture of 32%. The value of the strength of the FGM is only slightly higher than the tensile strength of Si-Bronze, by 10 MPa, suggesting that the Si-Bronze alloy controls tensile behavior of the bimetal. Tensile stresses axially applied on steel and copper are initially accommodated by the weaker material [16]. Afterwards, transfer of loading to the stronger and harder interfacial zone prevents further deformation and raises the stress level. For all 25 mm gauge length samples, fracture occurred outside the 9 mm interface length in the Si-Bronze region, which is indicative of the integrity of the diffusion zone, independent of the hot cracks formed (Figure 11p). This agrees with the suggested self-healing role of the liquid Si-Bronze, which filled the cracked HSLA steel. This robust performance was not observed in the work of Zhang et al. [16], where the bimetal specimen (without interlayer) failed at the interface between ER50-6 low alloy steel and HS211 Si-Bronze with a substantially lower strength than that of pure Si-Bronze. SEM imaging revealed the formation of deep dimples in addition to tear ridges and ripple walls, which is indicative of high plastic deformation during testing leading to ductile failure, as shown in Figure 15. No micro-cracking or porosities are visible. The tensile results provide evidence that both alloys can be strongly bonded together and can be used under tensile loading without interfacial failure.



**Figure 14.** Engineering stress–strain curves for three WAAM-ed samples: (a) unmixed HSLA steel, (b) HSLA steel/Si-Bronze FGM, and (c) unmixed Si-Bronze.

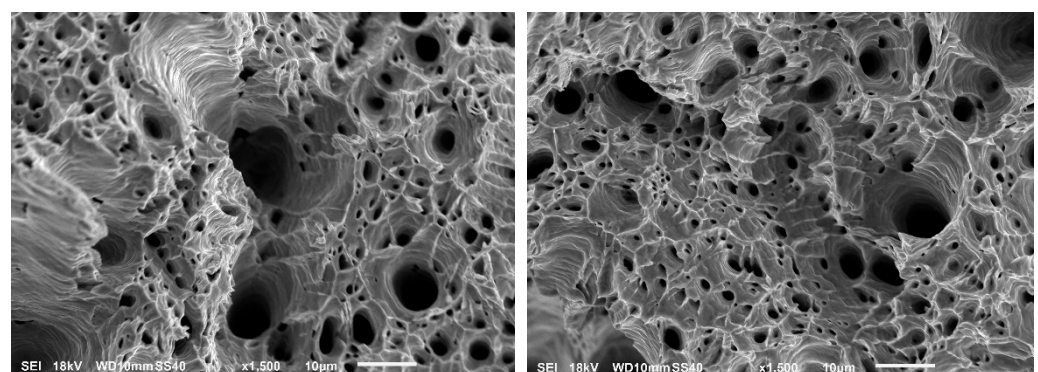


**Figure 15.** SEM micrographs of the fractured FGM specimen shown in Figure 14b.

#### 4.6. Three-Point Bending Test

The integrity of the interface between Si-Bronze and HSLA was further examined by employing a comparative three-point bending test, which was adapted from ASTM E290. The test setup is shown in Figure 4, where the interface line was aligned in parallel to the plunger such that during the test, the interface line would be plunged downwards. This would ensure the development of compressive and tensile stresses on either side of the specimen. Tensile stresses were expected to aid in rupturing the interface, thereby leading to the required fracture to stop the test. However, after testing three samples, the bimetal showed sliding behavior as the plunger traversed vertically. This sliding occurred such that the interface line was now displaced away from the plunger and substituted by an adjacent copper region (Figure 4b). Accordingly, the three test samples were displaced vertically to 30 mm before terminating the test. The maximum deflection location was 18 mm away from the interface boundary towards the Si-Bronze region. A flexural strength of  $350 \pm 15$  MPa was obtained. Figure 16 represents the flexural stress–displacement curve, where the slip of the tested specimen is evident at the discontinuities in the presented curve. Moreover, dye penetrant testing was performed on the specimens before and after applying the bending load. The test confirmed a crack-free surface before applying the bending load. However, a series of micro-cracks were developed on the tensioned surface after applying the bending load, as can be seen in Figure 17a. Figure 17b shows the tested specimen at a nearly  $90^\circ$  bending angle without failure, which can be attributed to the high ductility of Si-Bronze. This test has not been widely incorporated in the literature and is featured for the first time in this study for Si-Bronze/HSLA steel functionally graded materials. The results further demonstrate the mechanical integrity of the FGM interface.

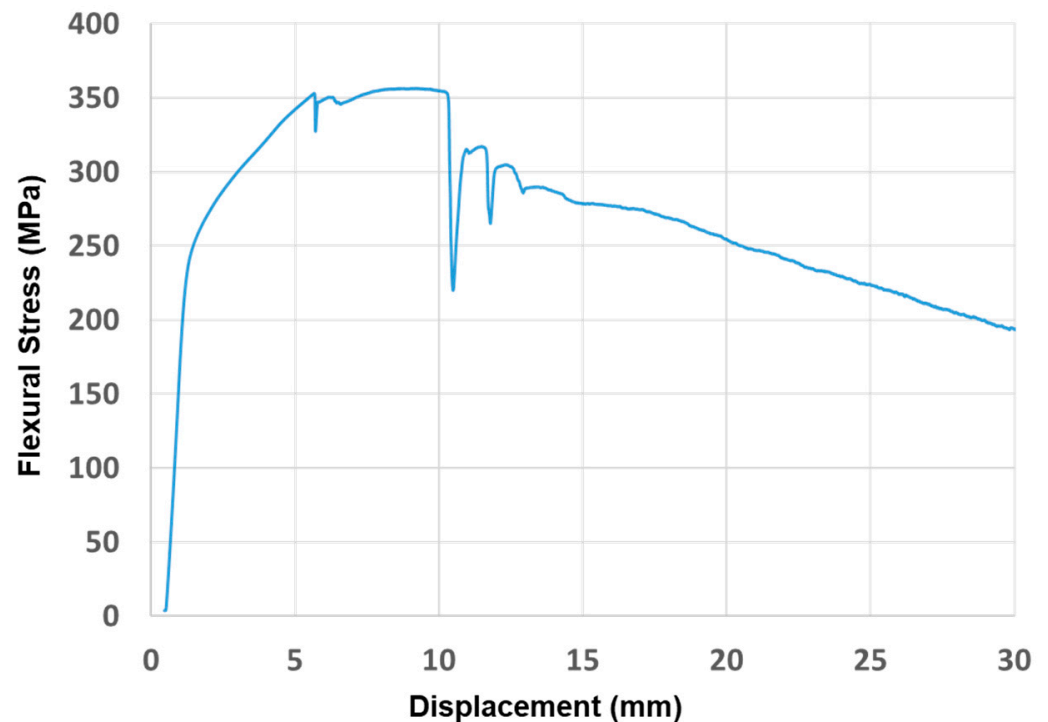
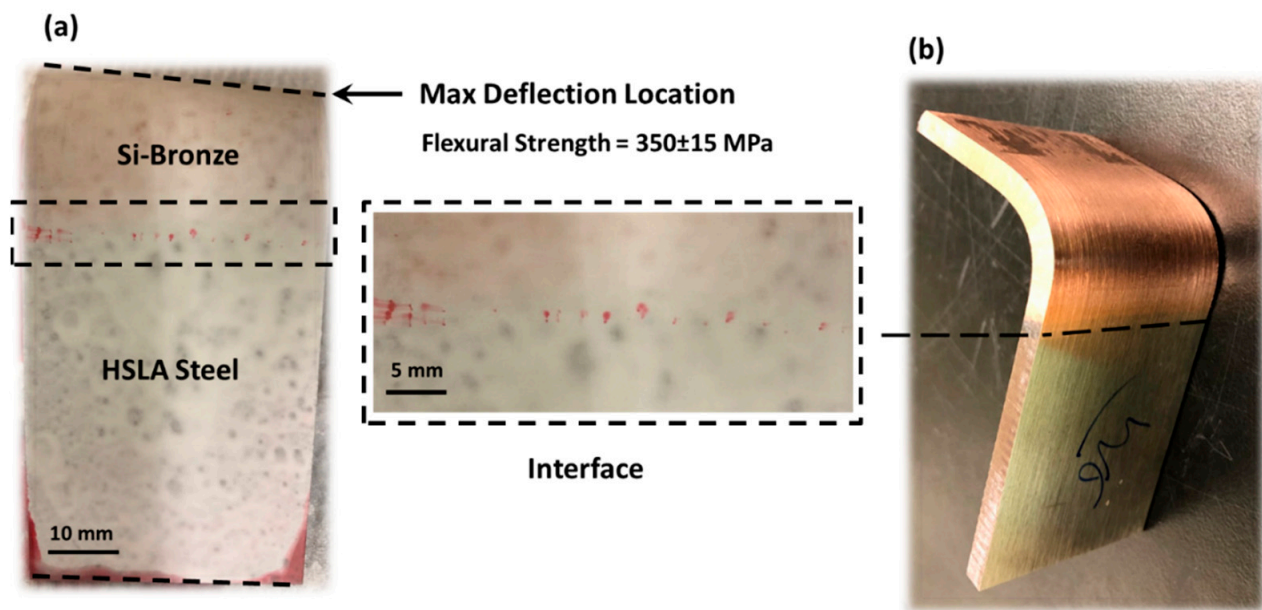


Figure 16. Flexural stress–average displacement curve for the bimetallic tested sample.



**Figure 17.** Three-point bending tested specimen (a) after dye penetrant test and (b) image of the specimen at 90° bending angle.

#### 4.7. Direct Shear Test

Unlike the uniaxial tensile test, the direct single shear test was applied locally at the interface boundary. Therefore, the shear test provides a direct assessment of the interface strength. The shear strength obtained was  $510 \pm 24$  MPa. This value is well above half the tensile strength of unmixed HSLA (950 MPa), which reflects the dominance of steel in the fracture behavior of the bimetal during shear. In contrast to the displayed tensile testing behavior, which was controlled by the Si-Bronze alloy, the direct shear test reflected the strength of the diffusion zone. This claim is also substantiated by the observed sheared surfaces, which were limited to the interface zone. Images taken from the shear bond tested samples are presented in Figure 18. Figure 18a,b show the two separated surfaces of the tested specimen in cross-sectional and side view, respectively. Red arrows represent the shear direction. Figure 18c,d show low-magnification SEM micrographs of cross sections of the fractured surfaces. Micro-cracks between the two dissimilar alloys are seen in Figure 18e (location “e” in Figure 18c) with bamboo-like features on the HSLA steel side. Figure 18f (location “f” in Figure 18c) shows a higher-magnification image of the fractured surfaces in the Si-Bronze region where elongated dimples are seen together with quasi-cleavage features and bamboo-like features. It is suggested that the micro-cracks were formed during the shear fracture due to the mismatch between the deformable Si-Bronze and HSLA steel (pointed out at the interface, Figure 18c). Sheared dimples (couplets) are dominant in the Si-Bronze regions of the fractured surfaces, indicative of the ductile shear dominating loading mode. On the other side of the examined fractured specimen (Figure 18g; location “g” in Figure 18d), flat and rugged facets are seen at the interface between HSLA steel and Si-Bronze. A high-magnification image of the HSLA steel region is shown in Figure 18h (location “h” in Figure 18g), where quasi-cleavage features are seen together with bamboo-like features [25]. It can be seen that the specimens failed in a mixed mode, revealing dimples as well as rubbed bamboo-like features [26]. The fracture mode was similar in all tested samples. The fractured interface is irregular in nature, which agrees with the irregular transition zone revealed by the optical microscopy panoramic view provided in Figure 7 [27,28].

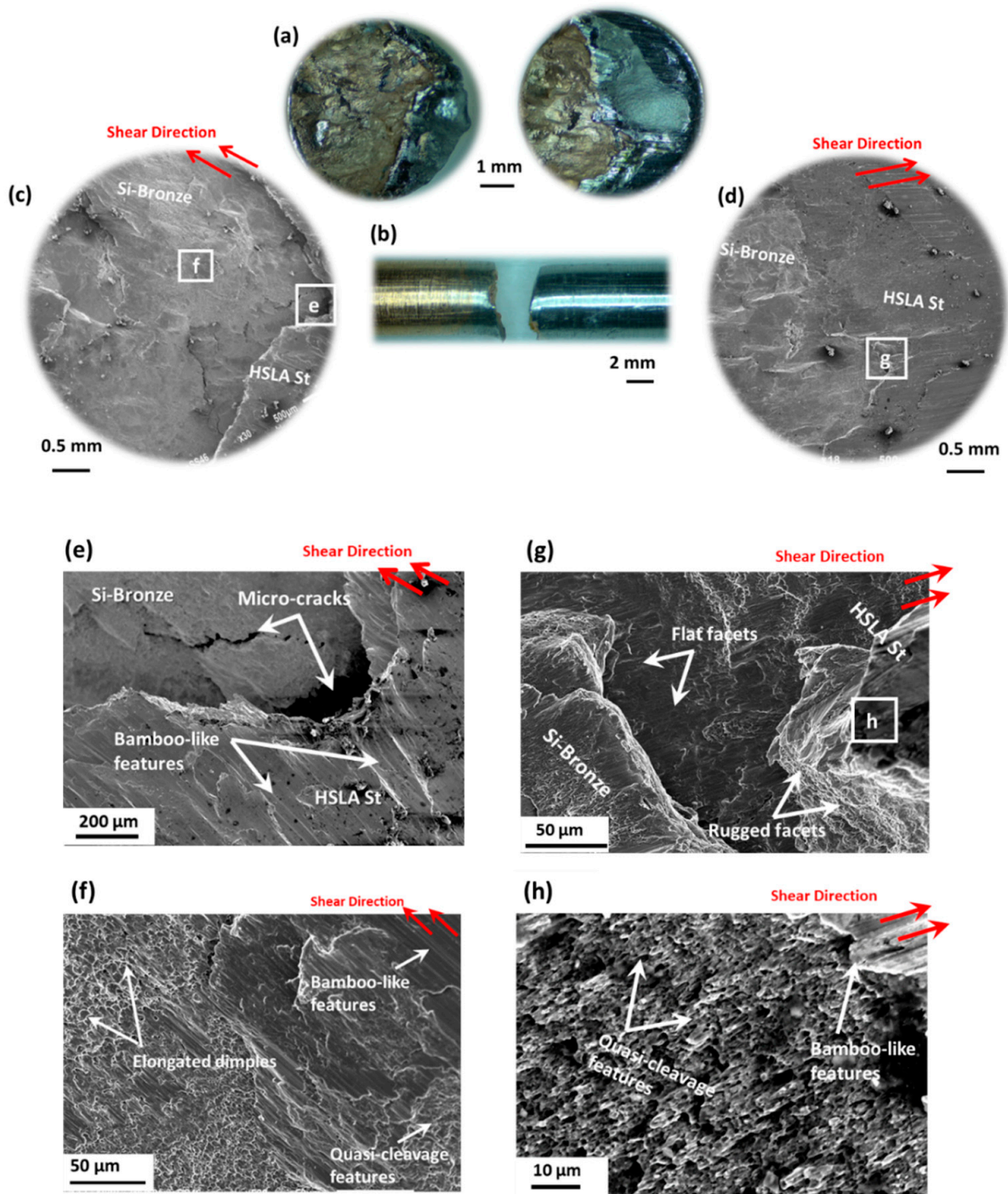


**Figure 18.** Fractured surfaces after the direct single shear tests. (a,b) Macro-images and (c–h) SEM micrographs at different magnifications.

## 5. Conclusions

In this study, bimetallic HSLA steel/Si-Bronze structures were fabricated using pulsed-GMAW-based WAAM. The challenges in joining the two dissimilar alloys are addressed. The microstructural evolution of the built structures, especially within the fusion zone, was investigated in relation to their mechanical properties. Several mechanical tests were performed to confirm the integrity of the interface. A summary of the obtained mechanical properties is presented in Table 4. The main conclusions are listed below:

1. The possibility of fabricating copper–steel FGMs using pulsed-GMAW-based WAAM has been proven.
2. No evidence for porosities throughout the entire samples (at the interface or in plain unmixed regions) was found.
3. Hot cracks appeared at the interface. Although they self-healed through filling with molten copper, they can be completely avoided by preheating the HSLA steel before subsequent copper deposition.
4. No intermetallic phases were identified within the interface zone between the two dissimilar alloys.
5. The hardness distribution suggests a gradual transition in mechanical properties.
6. Tensile failures occurred in the copper region, highlighting the integrity of the interface.
7. Tensile and bending behavior is dominated by Si-Bronze, while shear performance is controlled by HSLA steel.
8. Repeated heat cycles allowed the formation of a considerable interface length of 9 mm due to the diffusion of iron into the Si-Bronze region. EDS elemental analysis, microscopy, and mechanical characterizations validated the interfacial integrity.

**Table 4.** Summary of the obtained mechanical properties for the studied FGM.

Flexural Strength (MPa)	Shear Strength (MPa)	Tensile Results		
		YS (MPa)	UTS (MPa)	Elongation (%)
330 ± 15	510 ± 24	76 ± 9	164 ± 26	30 + 2

**Author Contributions:** Conceptualization, H.G.S., E.A.E.-D. and M.M.E.-H.; methodology, O.O., A.A.B. and M.M.E.-H.; software, A.A.B., O.O. and M.M.E.-H.; validation, H.G.S., E.A.E.-D., M.M.E.-H. and A.A.B.; formal analysis, H.G.S., A.A.B. and M.M.E.-H.; investigation, M.M.E.-H. and A.A.B.; resources, M.M.E.-H., A.A.B., O.O. and H.G.S.; data curation, M.M.E.-H., A.A.B. and H.G.S.; writing—original draft preparation, M.M.E.-H. and A.A.B.; writing—review and editing, H.G.S. and E.A.E.-D.; visualization, M.M.E.-H. and A.A.B.; supervision, H.G.S. and E.A.E.-D.; project administration, H.G.S.; funding acquisition, H.G.S., E.A.E.-D. and M.M.E.-H. All authors have read and agreed to the published version of the manuscript.

**Funding:** This research was funded by The American University in Cairo.

**Data Availability Statement:** Data are unavailable due to privacy or ethical restrictions.

**Acknowledgments:** The authors would like to thank the large team involved in the process development, sample preparation, and characterization, including colleagues and lab assistants from the Mechanical Engineering and Chemistry departments at The American University in Cairo, namely Ahmed Elsokaty, Farida Boulos, Mohamed Bakr, Hussein Abdelrazik, Abou-el-kassem Aly, Said Atta, and Emad Farag. The authors would like to express deep gratitude to Eng. Hala Salem for providing the necessary training and support for the sample preparation and micro-hardness facilities. The authors acknowledge the efforts of the materials testing lab team of the Mechanical Design and Production Engineering department, Cairo University, for their support in conducting the direct shear testing.

**Conflicts of Interest:** The authors declare no conflict of interest.

## References

1. Basinger, K.L.; Keough, C.B.; Webster, C.E.; Wysk, R.A.; Martin, T.M.; Harrysson, O.L. Development of a modular computer-aided process planning (CAPP) system for additive-subtractive hybrid manufacturing of pockets, holes, and flat surfaces. *Int. J. Adv. Manuf. Technol.* **2018**, *96*, 2407–2420. [[CrossRef](#)]
2. Da Silva, E.R.; Shinohara, A.C.; Nielsen, C.P.; de Lima, E.P.; Angelis, J. Operating Digital Manufacturing in Industry 4.0: The role of advanced manufacturing technologies. *Procedia CIRP* **2020**, *93*, 174–179. [[CrossRef](#)]
3. Mehrpouya, M.; Dehghanghadikolaei, A.; Fotovvati, B.; Vosooghnia, A.; Emamian, S.S.; Gisario, A. The potential of additive manufacturing in the smart factory industrial 4.0: A review. *Appl. Sci.* **2019**, *9*, 3865. [[CrossRef](#)]

4. Lockett, H.; Ding, J.; Williams, S.; Martina, F. Design for Wire+ Arc Additive Manufacture: Design rules and build orientation selection. *J. Eng. Des.* **2017**, *28*, 568–598. [[CrossRef](#)]
5. Popov, V.V.; Fleisher, A. Hybrid additive manufacturing of steels and alloys. *Manuf. Rev.* **2020**, *7*, 6. [[CrossRef](#)]
6. Xia, C.; Pan, Z.; Polden, J.; Li, H.; Xu, Y.; Chen, S.; Zhang, Y. A review on wire arc additive manufacturing: Monitoring, control and a framework of automated system. *J. Manuf. Syst.* **2020**, *57*, 31–45. [[CrossRef](#)]
7. Ščetinec, A.; Klobcar, D.; Bracun, D. In-process path replanning and online layer height control through deposition arc current for gas metal arc based additive manufacturing. *J. Manuf. Process.* **2021**, *64*, 1169–1179. [[CrossRef](#)]
8. Izham, E.D.I.A.; Alkahari, M.R.; Hussein, N.I.S.; Maidin, S.; Ramli, F.R.; Herawan, S.G. Online monitoring of wire arc additive manufacturing process: A review. *Adv. Mater. Process. Technol.* **2023**, 1–16. [[CrossRef](#)]
9. Pattanayak, S.; Sahoo, S.K. Gas metal arc welding based additive manufacturing—A review. *CIRP J. Manuf. Sci. Technol.* **2021**, *33*, 398–442. [[CrossRef](#)]
10. Dias, M.; Pragana, J.P.; Ferreira, B.; Ribeiro, I.; Silva, C.M. Economic and environmental potential of wire-arc additive manufacturing. *Sustainability* **2022**, *14*, 5197. [[CrossRef](#)]
11. Bandyopadhyay, A.; Zhang, Y.; Onuikwe, B. Additive manufacturing of bimetallic structures. *Virtual Phys. Prototyp.* **2022**, *17*, 256–294. [[CrossRef](#)]
12. Ayan, N.K.Y. Fabrication and characterization of functionally graded material (FGM) structure containing two dissimilar steels (ER70S-6 and 308LSi) by wire arc additive manufacturing (WAAM). *Mater. Today Commun.* **2022**, *33*, 104457. [[CrossRef](#)]
13. Bandyopadhyay, A.; Heer, B. Additive manufacturing of multi-material structures. *Mater. Sci. Eng. R Rep.* **2018**, *129*, 1–16. [[CrossRef](#)]
14. Dharmendra, C.; Shakerin, S.; Ram, G.J.; Mohammadi, M. Wire-arc additive manufacturing of nickel aluminum bronze/stainless steel hybrid parts—Interfacial characterization, prospects, and problems. *Materialia* **2020**, *13*, 100834. [[CrossRef](#)]
15. Rodrigues, T.A.; Bairrão, N.; Farias, F.W.C.; Shamsolhodaei, A.; Shen, J.; Zhou, N.; Maawad, E.; Schell, N.; Santos, T.G.; Oliveira, J.P. Steel-copper functionally graded material produced by twin-wire and arc additive manufacturing (T-WAAM). *Mater. Des.* **2022**, *213*, 110270. [[CrossRef](#)]
16. Liu, L.; Zhuang, Z.; Liu, F.; Zhu, M. Additive manufacturing of steel-bronze bimetal by shaped metal deposition: Interface characteristics and tensile properties. *Int. J. Adv. Manuf. Technol.* **2013**, *69*, 2131–2137. [[CrossRef](#)]
17. Velu, M.; Bhat, S. Metallurgical and mechanical examinations of steel-copper joints arc welded using bronze and nickel-base superalloy filler materials. *Mater. Des.* **2013**, *47*, 793–809. [[CrossRef](#)]
18. Zhang, M.; Zhang, Y.; Du, M.; Zhang, S.; Lei, L. Experimental characterization and microstructural evaluation of silicon bronze-alloy steel bimetallic structures by additive manufacturing. *Metall. Mater. Trans. A* **2021**, *52*, 4664–4674. [[CrossRef](#)]
19. Tomar, B.; Shiva, S. Microstructure evolution in steel/copper graded deposition prepared using wire arc additive manufacturing. *Mater. Lett.* **2022**, *328*, 133217. [[CrossRef](#)]
20. Elsokaty, A.; Oraby, O.; Sadek, S.; Salem, H.G. Influence of Wire Arc Additive Manufacturing Beads' Geometry and Building Strategy: Mechanical and Structural Behavior of ER70S-6 Prismatic Blocks. *J. Manuf. Mater. Process.* **2023**, *7*, 3. [[CrossRef](#)]
21. Queguineur, A.; Rückert, G.; Cortial, F.; Hascoët, J. Evaluation of wire arc additive manufacturing for large-sized components in naval applications. *Weld. World* **2018**, *62*, 259–266. [[CrossRef](#)]
22. Yildiz, A.S.; Davut, K.; Koc, B.; Yilmaz, O. Wire arc additive manufacturing of high-strength low alloy steels: Study of process parameters and their influence on the bead geometry and mechanical characteristics. *Int. J. Adv. Manuf. Technol.* **2020**, *108*, 3391–3404. [[CrossRef](#)]
23. Duarte, V.R.; Rodrigues, T.A.; Schell, N.; Santos, T.G.; Oliveira, J.P.; Miranda, R.M. Wire and arc additive manufacturing of high-strength low-alloy steel: Microstructure and mechanical properties. *Adv. Eng. Mater.* **2021**, *23*, 2001036. [[CrossRef](#)]
24. Sun, X.; Hao, W.; Geng, G.; Ma, T.; Li, Y. Solidification microstructure evolution of undercooled Cu-15 wt.% Fe alloy melt. *Adv. Mater. Sci. Eng.* **2018**, *2018*, 6304518. [[CrossRef](#)]
25. Martin, M.L.; Fenske, J.A.; Liu, G.S.; Sofronis, P.; Robertson, I.M. On the formation and nature of quasi-cleavage fracture surfaces in hydrogen embrittled steels. *Acta Mater.* **2011**, *59*, 1601–1606. [[CrossRef](#)]
26. Rao, N.V.; Sarma, D.; Nagarjuna, S.; Reddy, G.M. Influence of hot rolling and heat treatment on structure and properties of HSLA steel explosively clad with austenitic stainless steel. *Mater. Sci. Technol.* **2009**, *25*, 1387–1396. [[CrossRef](#)]
27. Kannan, A.R.; Kumar, S.M.; Kumar, N.P.; Shanmugam, N.S.; Vishnu, A.; Palguna, Y. Process-microstructural features for tailoring fatigue strength of wire arc additive manufactured functionally graded material of SS904L and Hastelloy C-276. *Mater. Lett.* **2020**, *274*, 127968. [[CrossRef](#)]
28. Shen, X.; Song, W.; Sevsek, S.; Ma, Y.; Hüter, C.; Spatschek, R.; Bleck, W. Influence of microstructural morphology on hydrogen embrittlement in a medium-Mn steel Fe-12Mn-3Al-0.05 C. *Metals* **2019**, *9*, 929. [[CrossRef](#)]

**Disclaimer/Publisher's Note:** The statements, opinions and data contained in all publications are solely those of the individual author(s) and contributor(s) and not of MDPI and/or the editor(s). MDPI and/or the editor(s) disclaim responsibility for any injury to people or property resulting from any ideas, methods, instructions or products referred to in the content.